RSC Advances

PAPER

View Article Online
View Journal | View Issue

Cite this: *RSC Adv.*, 2025, **15**, 50142

Enhanced thermoelectric performance of PEDOT:PSS/SWCNT/PDDA three-component composite films

Mustapha Adamu,[a] Muhammad Nadeem,[a] Muhammad Hasnain,[a] Asim Ullah,[a] Tafoor Afzal,[a] Na Fan,[a] Yuanrong Bao*[a] and Fei Jiao *[ab]

Conducting polymer/carbon nanocomposites represent a promising class of materials for flexible thermoelectrics, offering advantages such as low cost, solution processability, and low thermal conductivity. However, their performance is limited by high interfacial contact resistance at carbon nanomaterial junctions, which impedes charge transport and reduces electrical conductivity. To overcome this challenge, we employ poly(diallyldimethylammonium chloride) (PDDA) as a multifunctional interfacial architect, strategically designed to electrostatically bridge PEDOT:PSS and SWCNTs. Its role extends beyond dispersion to actively modulating energy filtering, reducing tunnelling barriers, and templating a favorable morphological landscape for charge transport. These morphological improvements facilitate efficient electron transport by reducing inter-nanotube junction resistance. This reduction in resistance enhances electrical conductivity while the refined interfaces simultaneously boost the Seebeck coefficient through energy-filtering effects, leading to a synergistic improvement in the power factor. The composite films, fabricated *via* layer-by-layer spray coating and mild annealing (100 °C, 10 minutes), achieved a remarkable electrical conductivity of 771 ± 45 S cm^{-1} and a Seebeck coefficient of 78 ± 9 μV K^{-1} at 55% PDDA, yielding a high power factor of 472 ± 40 μW m^{-1} K^{-2}. This work demonstrates that rational interfacial molecular design, rather than complex multi-layer structuring, is the key to unlocking high thermoelectric performance in organic composites. Our study provides a mechanistic blueprint for interface engineering, paving the way for the scalable production of efficient and flexible energy harvesting devices.

Received 23rd October 2025
Accepted 10th December 2025

DOI: 10.1039/d5ra08134c

rsc.li/rsc-advances

1. Introduction

Due to the global energy crisis, environmental challenges, and the fact that 60% of energy is wasted as heat, thermoelectric (TE) devices have shown promise as sustainable energy sources by directly converting waste heat into electricity. Organic thermoelectric (OTE) materials have emerged as particularly promising candidates for this application due to their low toxicity, mechanical flexibility, and cost-effective processing. However, their widespread implementation faces substantial challenges, including complex fabrication requirements and an inherently low power generation capacity compared to their inorganic counterparts. The energy conversion efficiency of TE materials is commonly evaluated using the dimensionless figure of merit (ZT), which is calculated from the electrical conductivity (σ), Seebeck coefficient (S), absolute temperature (T), and thermal conductivity (κ). For organic materials, κ is generally insignificant (<1 W m^{-1} K^{-1}); therefore, the power factor (PF = $S^2\sigma$) is often used as a substitute indicator to evaluate TE performance.[1,2] To increase the electrical conductivity of organic thermoelectric materials, charge carriers must be introduced through doping, as governed by the equation $\sigma = n\mu q$, where n is the charge carrier concentration, μ is the carrier mobility, and q is the elementary charge. To achieve the highest power factor, the relationship between σ and S must be optimized. This is commonly accomplished by increasing n to values within the range of 10^{26} m^{-3} to 10^{27} m^{-3} and selecting optimal dopants.[3,4]

Recent developments in OTE materials have centered on the strategic engineering of interfacial interactions within nanocomposite architectures.[5] This paradigm shift recognizes the exceptional potential of hierarchical assemblies combining conductive polymers with carbon nanomaterials (*e.g.*, graphene, carbon nanotubes), which spontaneously form three-dimensional conjugated networks (3D networks) during solution processing and thin-film deposition. Such nanostructured systems exhibit dramatically enhanced thermoelectric

[a]*State Key Laboratory of Advanced Materials for Intelligent Sensing, Tianjin Key Laboratory of Molecular Optoelectronic Science, Department of Chemistry, School of Science, Tianjin University, Tianjin, 300072, China. E-mail: feijiao@tju.edu.cn; baoyr@tju.edu.cn*

[b]*Collaborative Innovation Centre of Chemical Science and Engineering, Weijin 92, Tianjin, 300072, China*

performance compared to their individual components, achieving this through synergistic effects that simultaneously optimize electrical conductivity while preserving favorable Seebeck coefficients.[6,7] The formation of these percolating 3D networks enables unprecedented charge transport pathways while maintaining nanoscale phase separation a critical feature that minimizes thermal conductivity through enhanced phonon scattering.

Research focuses on precisely controlling these interfacial interactions through molecular design, processing optimization, and advanced characterization techniques, with the ultimate goal of establishing design rules for next-generation OTE materials capable of bridging the performance gap with inorganic thermoelectrics.[8] This approach not only advances fundamental understanding of charge-energy transport in organic hybrids but also opens new avenues for scalable manufacturing of flexible, high-performance thermoelectric devices.

Study has demonstrated that among various preparation methods for organic thermoelectric materials, layer-by-layer (LbL) assembled composites exhibit significantly higher power factors compared to conventionally mixed nanocomposites. This enhanced performance stems from superior nanostructural interconnectivity achieved through the LbL fabrication approach.[9,10] LbL assembly technique has emerged as a powerful platform for fabricating precisely engineered thin films with tunable thermoelectric and mechanical properties. This versatile approach involves cyclic deposition of complementary materials from aqueous solutions, exploiting various intermolecular interactions including electrostatic forces, hydrogen bonding, and π–π stacking.[11,12] The method enables nanoscale control over film architecture and composition, accommodating diverse building blocks such as polyelectrolytes, nanoparticles, conjugated polymers, and clays on various substrates. Furthermore, the assembly process can be precisely modulated by adjusting experimental parameters including ionic strength, pH, and temperature, allowing fine control over film thickness and functional properties.[13,14] These variables directly influence interlayer interactions, molecular packing density, and charge transport pathways, thereby determining the film's mechanical flexibility, chemical stability, and ultimately, its thermoelectric performance.[15–17] Thermoelectric films composed of single and multi-walled carbon nanotubes (MWNTs), stabilized by polymeric surfactants such as poly(3-hexylthiophene), achieve power factors comparable to commercial bismuth telluride (Bi_2Te_3) at near room temperature conditions. These hybrid systems exhibit a concurrent enhancement in both Seebeck coefficient and electrical conductivity with increasing deposition cycles, attributed to improved charge carrier mobility within the nanostructured network.[18–20]

Enhancing the thermoelectric performance of PEDOT:PSS films relies on strategies that promote phase segregation between PEDOT and PSS, thereby extending electron conduction pathways. PEDOT:PSS is a water-soluble, intrinsically conductive polymer complex that has been widely used as a p-type organic thermoelectric material, prepared through the polymerization of EDOT in the presence of PSS.[21] Water solubility is due to the ionic stabilization PSS imparts to the conductive and hydrophobic PEDOT, which adopts a coiled conformation in water with a PSS shell encapsulating a PEDOT core. This core–shell structure demonstrates significantly poor thermoelectric performance when deposited on glass substrates.[22] The removal of PSS from PEDOT reduces interchain spacing between conductive polymer backbones. Polar solvent treatment (*e.g.*, ethylene glycol or dimethyl sulfoxide) facilitates PSS dissociation, significantly enhancing electrical conductivity.[23]

Present breakthroughs have demonstrated that even insulating polymers when strategically incorporated into CNT-based composites can dramatically enhance thermoelectric performance. Notably, a CNT/polystyrene composite recently achieved a remarkable power factor of 413 $\mu W\ m^{-1}\ K^{-2}$, surpassing previous records for CNT/conductive polymer systems. This finding challenges conventional design paradigms by proving that non-conductive matrix polymers can actively improve thermoelectric performance rather than merely serving as passive binders.[24,25] Recent studies suggest that the limitations of conventional processing approaches may be overcome by innovative strategies such as molecular doping, nanoscale phase control, and hybrid organic TE composite design. These advancements aim to bridge the performance gap while retaining the intrinsic advantages of organic thermoelectrics.[26,27]

Layer-by-layer assembly is noted for its ability to control morphology, thereby reducing contact resistance and enhancing thermoelectric performance. However, many other high-performance methods face scalability issues due to their reliance on numerous deposition cycles.[28] Herein, we demonstrate that exceptional performance can be achieved with a simplified, optimized bilayer architecture, highlighting the paramount importance of interface quality over the sheer number of interfaces. To realize this, we introduced PDDA as a multifunctional additive into the SWCNT suspension prior to LbL deposition. PDDA serves as a multifunctional additive in SWCNT-based thermoelectric composites.[29,30] It acts as a capping agent to modulate the SWCNT morphology, preventing aggregation while enhancing surface crystallinity and mitigating grain boundary defects. The presence of PDDA in the composites also stabilised the SWCNT interfaces during formation. The thermoelectric properties of a bilayer (BL) thin film were analyzed as a function of the concentration of PDDA. A BL PEDOT:PSS/SWNT–PDDA composite film with 55% of PDDA (43 nm thick) exhibits an electrical conductivity of $771 \pm 45\ S\ cm^{-1}$ and a Seebeck coefficient of $78 \pm 9\ \mu V\ K^{-1}$, which results in a power factor of $472 \pm 40\ \mu W\ m^{-1}\ K^{-2}$. This outstanding power factor is attributed to improved dispersion and electrostatic attraction between cationic PDDA and anionic PSS chains, which collectively yield high electrical conductivity while maintaining the Seebeck coefficient. The study demonstrates an effective fabrication method for high-performance OTE materials with promising applications in energy harvesting systems.

2. Experimental section

2.1 Materials

Poly(diallyldimethylammonium chloride) (M_w = 200 000–350 000 g mol^{-1}, 20 wt% aqueous solution) was purchased from

Sigma Aldrich. Poly(3,4-ethylenedioxythiophene):poly(styrenesulfonate) (PEDOT:PSS) Clevios PH1000 was purchased from Heraeus Materials Technology (Shanghai) Ltd. Dimethyl sulfoxide (DMSO) and isopropyl alcohol (99%) were purchased from Innochem Nanotechnology Company China Limited. All chemicals were used as received without further treatment.

2.2 Preparation of PEDOT:PSS/SWCNT–PDDA suspensions

50 μl of DMSO was added to 950 μl of PEDOT:PSS (Clevios PH1000), to prepare PEDOT:PSS–5% DMSO solution. The solution was stirred for one hour and then filtered through a 0.45 μm PVDF syringe filter into a flask. The solution was then stirred vigorously for a further 5 minutes to ensure homogeneity. 5 mL of SWCNT suspension was measured and placed in cleaned glass bottles. To the first sample, 4 mL of PDDA was added to obtain a homogeneous PDDA–SWCNT solution. This solution was bath-sonicated for 30 minutes, followed by 30 minutes of mechanical stirring to ensure the suspension was fully homogenised. The same procedure was then repeated for the remaining four samples by adding 5 mL, 6 mL, 7 mL and 8 mL of PDDA respectively, which correspond to PDDA contents of 44%, 50%, 55%, 58% and 62% (in the order of 4 mL, 5 mL, 6 mL, 7 mL and 8 mL additions).

2.3 Layer-by-layer films assembly

Before the spray coating process, glass substrates measuring 10 × 10 mm in area with a thickness of 0.5 mm were cleaned with detergent, deionized water, isopropyl alcohol, and acetone. After the solvents were removed, the substrates were dried with nitrogen gas and subjected to plasma treatment for 10 minutes. Subsequently, a 4 nm layer of chromium followed by a 30 nm layer of gold were evaporated onto the glass substrates using physical vapor deposition to form electrodes. Prior to film deposition, the electrodes were plasma-treated (using an Atto Plasma System, Thierry, Royal Oak, MI) to impart a negative surface charge. Layer-by-layer (LbL) assembly was conducted using a spray coating machine (model HO TH-04). The ultrasonic vibration frequency of the nozzle was set to 40 kHz, with a distance of 35 mm set between the substrate and the nozzle tip. The lateral nozzle velocity was set to 45 mm s^{-1}. The ultrasonic nozzle tip was configured to produce droplets averaging 55 μm in size. The spray was then smoothly directed onto the glass substrate with the aid of carrier air at a moderate pressure of 0.3 MPa, which prevented the droplets from scattering in the air. First, the PEDOT:PSS solution was sprayed as a background layer onto the cleaned glass substrate (see Fig. S1–S3). This process was repeated three times for 30 seconds and then dried with air pressure. The above procedure was then repeated for the SWCNT–PDDA solution to deposit a second layer of thin composite film containing 44%, 50%, 55%, 58% and 62% PDDA by volume at room temperature. Finally, the two-layer thin film was annealed at 100 °C on a hot plate for 10 minutes and then left to cool at room temperature, as shown in Fig. 1.

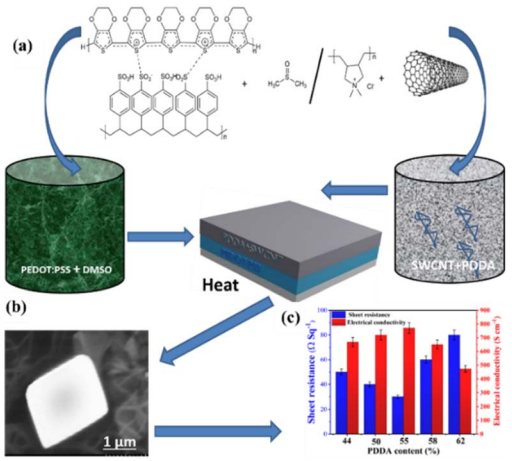

Fig. 1 (a) Schematic view for the formation of bilayer composite film assembly. (b) SEM image of composite film as a function of PDDA content. Scale bar: 1 μm. (c) Graph of sheet resistance and conductivity as a function of PDDA content.

2.4 Film characterization

Thickness of films deposited on glass substrate was measured by using profilometer (Fig. S4). Raman spectra of bilayer films were collected using a Jobin-Yvon Horiba Labram HR spectrometer (Piscataway, NJ) with a 514.5 nm ion laser and Olympus BX41 microscope (Waltham, MA). Film topographies were analyzed *via* atomic force microscopy (AFM; Bruker, Billerica, MA) using HQ: NSC35/AI BS probes (force constant: 5.5–16 N m^{-1}), and scanning electronic microscopy (SEM). XPS spectra of bilayer films were acquired using an Omicron XPS/UPS system (Denver, CO) with a monochromatic Mg Kα source (DAR) at 0.8 eV resolution. Absorption spectra were analyzed *via* UV-vis-NIR spectroscopy. Surface roughness was quantified using the Nanoscope Analysis software system. Internal microstructure of the composite film was analysed by using TEM. EDS elemental distribution maps were analysed using high resolution transmission electron microscope (HRTEM).

2.5 Thermoelectric measurements

To measure the thermoelectric performance of the thin films, we used a homemade van der Pauw four-probe system. The system, provided by Beijing Vector Tonghui Technology Co., Ltd., uses two probes to supply a constant current while the other two monitor the voltage. The apparatus is integrated with a motor to create a vacuum through suction. All thermoelectric properties, including electrical conductivity and the resistance, were measured at room temperature (~298 K) using an instrument with heating plates spaced 4 mm apart. The four-probe machine was set at an operating voltage of not more than 10 volts concerning the applied current to examine the thermoelectric properties of PEDOT:PSS/SWCNT–PDDA films (Fig. S5). The probe tips used in this TE analysis were 0.4 mm in diameter with a distance of 1.0 mm between the tips.

The Seebeck coefficient was determined using a homemade Seebeck measurement system. All measurements were repeated five times, and the average values were used for analysis. The sheet resistance of the thin films was calculated utilizing $R_s = 4.23(V/I)$, where 4.23 is known as the correction factor based on the dimensions of the films with respect to the distance between probes tips.[27] Temperature dependent resistance data were obtained utilizing a commercial instrument known as Dynacool Physical Property Measurement System (PPMS) (Quantum Design, san Diego, CA) using a four-point probe setup. The resistivity was calculated by multiplying the measured resistance by the ratio of the area divided by the length of the sample.

3. Results and discussion

3.1 Material and characterization

Fig. 1 presents the chemical structures of the components used and schematic view for the formation of bilayer composite film assembly. The LbL films were constructed using PEDOT:PSS and PDDA-functionalized SWCNT as a model system, chosen for their demonstrated excellent thermoelectric properties. In this system, PEDOT:PSS served dual roles as both the conductive component and an anionic polymeric surfactant. SWCNTs were selected for their high electrical conductivity and stability, while PDDA functioned as both a binding agent and dispersant for the SWCNT.

3.2 Morphology and microstructure characterization

The properties governing charge transport are primarily influenced by the domain structure and molecular arrangement. AFM and SEM were used to study the surface morphology of the composite film as a function of PDDA content. This technique directly probed the surface properties of PEDOT:PSS/SWCNT–PDDA films through structural and morphological analysis. AFM images revealed that the addition of PDDA altered the composite film's surface topology, and this induced morphological refinement that enhanced electron transport. Further increases in PDDA concentration resulted in progressively greater surface roughness, as measured by the root mean square (RMS) value. The RMS values rose from 7.6 nm to 20.3 nm for composite films containing PDDA content (%). This increase is attributed to the formation of a cross-linked network between crystalline and amorphous phases, caused by the control of polymer chains during PDDA incorporating, as depicted in Fig. S6. At moderate PDDA loadings (44–55%), further roughness improvements resulted in enhanced electrical conductivity through optimized charge transport pathways. These rougher surfaces originate from distended SWCNT bundles, resulting from PSS depletion reducing nanotube stabilization in solution. Critically, larger bundles decrease inter-junction distances between nanotubes, enhancing electron transport through improved percolation pathways. This mechanism is corroborated by the reduced T_0 values derived from 3D variable-range hopping (VRH) modeling, confirming facilitated charge transport.[31]

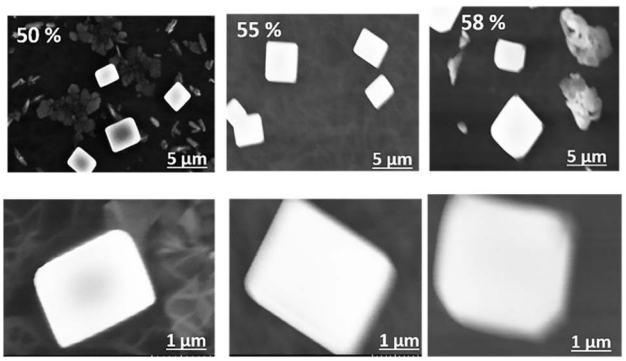

Fig. 2 Scanning Electron Microscopy (SEM) images showing the morphology of PEDOT:PSS/SWCNT–PDDA composite films as a function of PDDA content. Scale bars: 1 μm and 5 μm.

SEM images of the prepared PEDOT:PSS/SWCNT–PDDA composite films at varying weight ratios (50–58% PDDA) were acquired at two magnification scales (1 μm and 5 μm), as shown in Fig. 2. Statistical analysis of multiple scanned regions revealed a consistent decrease in SWCNT bundle diameters with increasing PDDA content across all tested composites films at different ratios. This morphological and structural transformation was attributed to enhanced electrostatic interactions between PEDOT:PSS and SWCNT–PDDA, which improved dispersion and altered the composite's microstructure. These attractive intermolecular forces modify the electronic structure, thereby enhancing charge carrier mobility and ultimately improved thermoelectric performance. Furthermore, when PDDA was introduced to SWCNT with identical concentrations, we observed a reduction in bundle diameter, demonstrating PDDA's role in improving SWCNT dispersion. This improved dispersion resulted in decreased sheet resistance and enhanced electrical conductivity, as supported by Fig. 1c.

The distribution of components and the nature of interfacial interactions within the composite material, following the strategic addition of a SWCNT–PDDA layer onto a pre-existing PEDOT:PSS film, were meticulously assessed using transmission electron microscopy (TEM). This advanced imaging technique is particularly well-suited for such analysis as it provides direct visual evidence of nanoscale morphology, phase

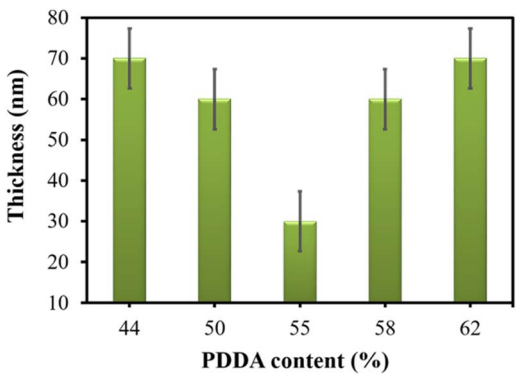

Fig. 3 Film thickness as a function of PDDA loading (%).

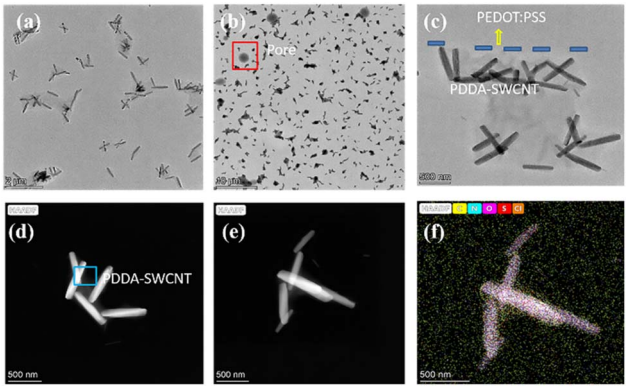

Fig. 4 Electron-microscopy analysis rationalising the high thermoelectric performance of the PEDOT:PSS/SWCNT–PDDA film. (a) Low-magnification TEM overview (2 μm). (b) HRTEM micrograph showing pore morphology (10 μm). (c) A clear heterointerface between the two polymers, interfacial TEM image (500 nm). (d and e) HAADF-STEM images (500 nm) of the blue-boxed area revealing nanometre-scale crystallites from two viewing angles. (f) Corresponding EDS maps of C, N, O, S and Cl elemental distributions. The base elements of C, S and O originated from PEDOT:PSS, SWCNT and the additional Cl and N elements were ascribed to PDDA, respectively.

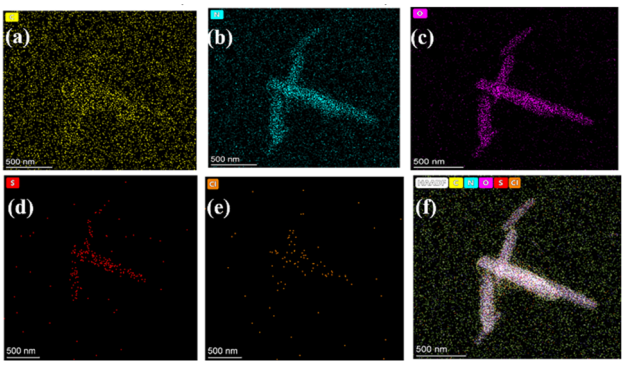

Fig. 5 EDS elemental distribution maps of the PEDOT:PSS/SWCNT–PDDA film: (a) carbon, (b) nitrogen, (c) oxygen, (d) sulphur, (e) chlorine and (f) EDS image of HAADF group distribution. All images were captured with a scale bar of 500 nm.

distribution, and the quality of interfacial contact between different materials. The obtained TEM images, presented in Fig. 4, collectively confirm the successful and uniform coating of both functional layers on the substrate without significant delamination or large-scale aggregation. To analyse the internal microstructure of the composite films, lamellar TEM samples were prepared using focused ion beam (FIB) technology. A key observation from this analysis is visible in Fig. 4b, small pores (red square) were observed in composite films, likely due to the incomplete decomposition of PDDA. The observed pores intensify phonon scattering and thereby lower the film's κ, underscoring how structural engineering further suppresses thermal conductivity consistent with ZT and κ calculations reported in many studies that use cationic polyelectrolytes, as detailed in Note S7.

Fig. 4c, which reveals a well-defined and continuous heterointerface between the lighter PEDOT:PSS region and the darker SWCNT–PDDA layer. This distinct boundary suggests a coherent and intimate contact between the two polymers, which is crucial for efficient charge transfer and mechanical integrity within the composite structure. Furthermore, high-resolution TEM (HRTEM) imaging was employed to probe the atomic-level structure of the film. The resulting HRTEM micrograph (Fig. 4d) demonstrated the high crystallinity of the PEDOT:PSS/SWCNT–PDDA composite, showcasing clear lattice fringes that correspond to the graphitic structure of the SWCNT within the PDDA matrix. This crystalline order is a critical factor for enhancing the electrical conductivity and overall electrochemical performance of the composite film, confirming that the fabrication process successfully preserved the intrinsic advantageous properties of the SWCNTs.

Fig. 5 displayed the EDS distribution of C, N, O, S and Cl elements, respectively. The distribution of N (Fig. 5b) was consistent with that of S (Fig. 5d), mainly due to the surfaces of PEDOT:PSS being coated with SWCNT–PDDA. Overall, the comprehensive TEM analysis suggested that the excellent thermoelectric performance of the PEDOT:PSS/SWCNT–PDDA films arose from a synergistic microstructural evolution. The effective coating and dispersion by PDDA reduced SWCNT bundling and pore size while introducing a high density of interfaces, a morphology that established efficient charge transport pathways and significantly enhanced σ. Simultaneously, these newly formed heterointerfaces enhanced energy-dependent carrier scattering, leading to a higher S. Furthermore, the residual pores, transition grain boundaries, and dislocations within the composite acted as effective phonon scattering centers, thereby suppressing the κ. This concurrent optimization of electrical and thermal transport properties culminated in the superior thermoelectric performance.

Film composition, binding energy, and surface chemistry were analyzed by XPS under UHV (9×10^{-8} torr, 90° take-off angle). Detection of C, N, Cl, O and S enabled tracking of

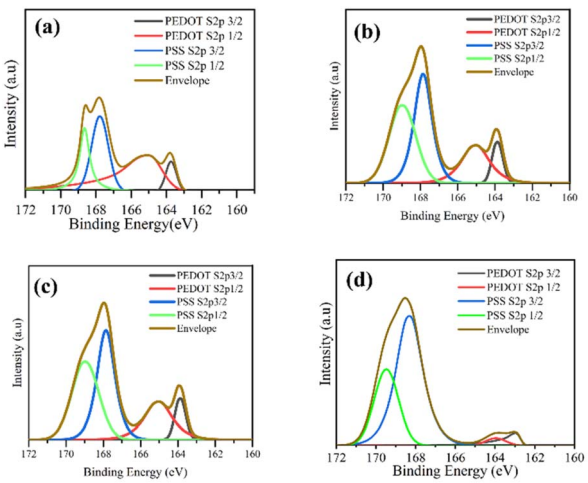

Fig. 6 XPS spectra of PEDOT:PSS/SWCNT films after the addition of PDDA at concentrations of (a) 44%, (b) 50%, (c) 55% and (d) 58%.

Table 1 Atomic percentage of each element analysed within the PEDOT:PSS/SWCNT–PDDA films at different PDDA content (%)

Element	44% PDDA	50% PDDA	55% PDDA	58% PDDA
S	0.4	1.61	1.36	1.57
C	80.99	67.68	70.23	67.37
N	1.19	1.43	1.99	5.61
Cl	1.51	1.45	6.25	5.35
O	17.42	27.77	24.97	19.2

chemical state evolution with PDDA content (Fig. 6). XPS confirmed the elemental composition and chemical states of the films. The consistent N 1s peak at 402 eV in all spectra verifies successful SWCNT–PDDA layer formation on glass substrates and bonded to the PEDOT:PSS layer. Deconvolution of the C 1s spectrum (SWCNT–PDDA layer) revealed five bands: C=C (284.48 eV), C–C (284.51 eV), C–O (284.89 eV), C=O (284.78 eV) and O=C–OH (285.09 eV), respectively. The five-band deconvolution was consistently observed in all composite films containing PDDA. XPS quantification revealed that the atomic percentage of C–N bonds increased with higher PDDA content, with values of 1.19% (44%), 1.43% (50%), 1.99% (55%) and 5.61% (58%) (Table 1). This trend indicates that the prepared films underwent a change in their electronic density of states as the PDDA volume ratio increased, confirming enhanced interfacial interactions. Concurrently, the S 2p spectra showed a reduced PEDOT peak intensity at 50–58% PDDA, indicating a molecular conformation transition that disrupts charge transport and reduces electrical conductivity at high PDDA content.[32] The phase splitting spectrum of the PSS spectra shows a high-intensity band at 168 eV and 169 eV, corresponding to the spin splitting of the sulfur atom from the PSS chains.[33,34] However, the S 2p nuclear spectra were observed at 166 eV and 167 eV binding energies due to the spin splitting of the sulfur atom from the PEDOT.[35,36] The PEDOT peak intensity changed reflects structural modifications in PEDOT which corroborates the corresponding doping level shifts, as depicted in Fig. 6 and Table 1.

3.3 Thermoelectric performance

To assess the effects of PDDA doping, we evaluated the thermoelectric performance as a function of its concentration. The reliability of our measurement system was first verified using a standard PEDOT:PSS film. Five repeated measurements of this standard yielded Seebeck coefficients of 18–20 μV K^{-1} and electrical conductivities of 900–1000 S cm^{-1}, confirming good repeatability. Electrical conductivity rose from 580 ± 35 S cm^{-1} (44% PDDA) to 600 ± 65 S cm^{-1} (50% PDDA). A maximum conductivity of 771 ± 45 S cm^{-1} was achieved at 55% PDDA and then modestly decreased to 380 ± 35 S cm^{-1} and 100 ± 20 S cm^{-1} (at 58–62% PDDA). The maximum electrical conductivity of 771 ± 45 S cm^{-1} was attributed to effective dispersion of SWCNT at moderate concentrations, PDDA reduces PEDOT:PSS/SWCNT film thickness but boosts conductivity (Fig. 3). This inverse trend reflects PDDA ability in enhanced SWCNT dispersion, minimizing interfacial contact resistance. Notably, at high PDDA content electrical conductivity decreased, attributed to aggregating of PDDA, resulting in a lower electrical conductivity.

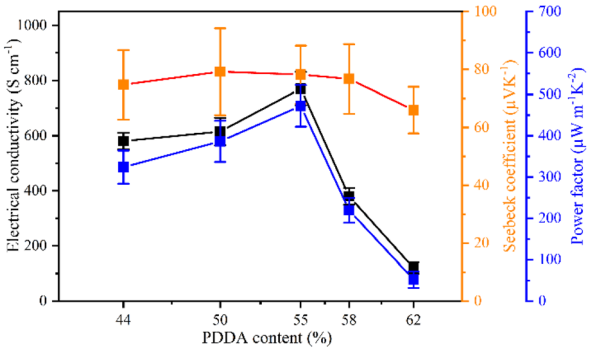

Fig. 7 TE performance of the PEDOT:PSS/SWCNT–PDDA composite films as a function of PDDA concentration.

The Seebeck coefficient and power factor as a function of PDDA concentration is shown in Fig. 7. Interestingly, the maximum Seebeck coefficient of 80 ± 13 μV K^{-1} is achieved at 50% PDDA. The value of the Seebeck coefficient steadily decreases to 78 ± 9 μV K^{-1} at 55% PDDA content and 65 ± 7 μV K^{-1} at 62%, respectively. It suggests that PDDA induces an improvement in the Seebeck coefficient owing to the improvement of the energy filtering effects at the PEDOT:PSS and SWCNT–PDDA interface.[34] The optimal composition of 55% PDDA yielded a maximum power factor of 472 ± 40 μW m^{-1} K^{-2}. This performance is competitive with and often superior to that of more-complex multilayer architectures, as detailed in Tables S1 and S2. Critically, the conductivity improvement occurred with only a minor Seebeck coefficient reduction (80 ± 13 to 78 ± 9 μV K^{-1}), demonstrates an effective decoupling of these typical correlated parameters, as depicted in Fig. 7.

3.4 Electron vibration and charge transfer behaviour

Raman spectroscopy (532 nm) was employed to evaluate electron transfer behaviour, chain structure variations, and interfacial π–π interactions in PEDOT:PSS/SWCNT–PDDA

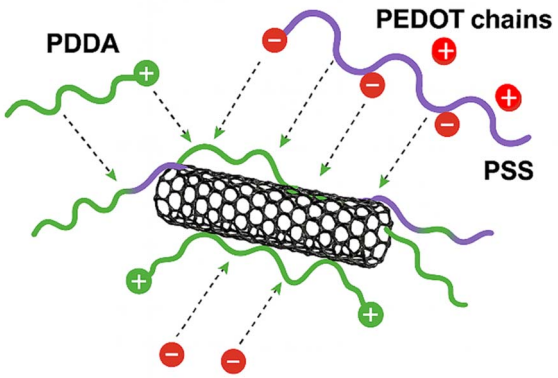

Fig. 8 Schematic of electrostatic interaction mechanism between PDDA, SWCNT and PEDOT:PSS.

composites. Bands at 1591 cm^{-1} (C_α=C_β), 1341 cm^{-1} (C_α–C_β) and 1344 cm^{-1} (C_α–$C_{\alpha'}$) corresponded to symmetric stretching vibrations. The G-band shifted from 1590 to 1432 cm^{-1} with narrowed peak intensity confirmed structural reorganization, as depicted in Fig. 9a. Concurrently, the C_α–C_β symmetric stretching vibration shifted from 1341 cm^{-1} to 1344 cm^{-1}, while its intensity decreased at high PDDA loading. These spectral changes indicate a change in PEDOT's structure, consistent with decreases in conductivity at high PDDA content. The PDDA loading-induced shifts in PEDOT peak positions reflect structural reorientation and conformational changes between polymer chains due to electrostatic interactions. These electrostatic interactions alter the new interfaces to enhance energy-dependent carrier scattering, thereby enhancing charge transport, carrier mobility, and thermoelectric performance. The mechanism involves a single-step electrostatic self-assembly. The polycation PDDA acts as a molecular glue, using its positive charges to bridge the COO^- groups on acid-oxidized SWCNTs and the SO_3^- groups on the PSS component of PEDOT:PSS. This directly anchors the conducting polymer sheath to the nanotube, as shown in Fig. 8. Mechanical stability is further confirmed by Raman spectroscopy, negligible changes in the I_D/I_G ratio before/after PDDA incorporation (Fig. S7), indicate preserved structural integrity.

UV-vis-NIR spectroscopy was used to examine the absorption spectra of composite films and to probe SWCNT–PDDA/PEDOT interfacial interactions. Both pristine SWCNTs and the composite film exhibited a distinct at 900 nm absorption band, attributed to the PDDA-modified morphology, which creates more continuous pathways for charge carriers between the PEDOT:PSS and SWCNT–PDDA layers.[37] PDDA is recognised cationic polyelectrolyte that non-covalently functionalizes carbon nanotubes *via* π–π interactions, thereby enhancing their processability and integration into composite matrices.[38,39] The composite film exhibited significantly reduced absorption intensity against PEDOT:PSS/SWCNT composites film before PDDA is added, this indicates stronger interlayer electronic coupling, as shown in Fig. 9b.[35] This effect intensified in composites films contained PDDA, confirmed more robust PEDOT:PSS/SWCNT–PDDA interfacial interactions.[40,41] For the composite films contained PDDA, the intensities of the absorption peaks were all reduced with increases in PDDA content.

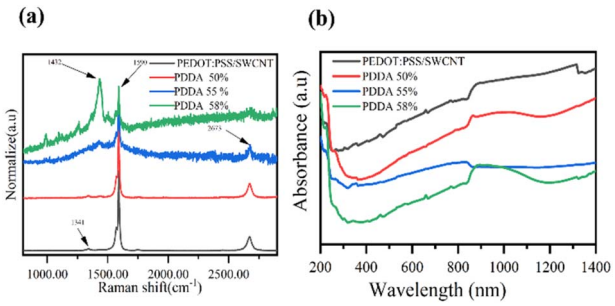

Fig. 9 (a) Raman spectra of PEDOT:PSS/SWCNT films before and after treatment with PDDA at concentrations of 0%, 50%, 55% and 58%. (b) UV-vis-NIR absorption spectra of PEDOT:PSS/SWCNT films before and after treatment with PDDA at concentrations of 0%, 50%, 55% and 58%.

4. Conclusions

In conclusion, this work successfully addresses the critical challenge of interfacial resistance in polymer/CNT composite by introducing PDDA as a multifunctional interfacial architect. Our approach transforms a performance-limiting interface into a performance-enhancing one, enabling a synergistic boost in both electrical conductivity and the Seebeck coefficient. The resulting power factor of 472 ± 40 μW m^{-1} K^{-2}, achieved *via* a simple and scalable process, proves that rational molecular design at the interfaces not structural complexity is the key to superior thermoelectric performance. This paradigm shift provides a scalable and effective blueprint for the future development of high-performance, flexible organic thermoelectrics.

Author contributions

Writing-original draft, software, investigation, conceptualization: [Mustapha Adamu]. Data curation: [Muhammad Nadeem]. Data curation: [Muhammad Hasnain]. Conceptualization: [Asim Ullah]. Formal analysis: [Na Fan]. Formal analysis: [Tafoor Afzal]. Formal analysis and writing-review: [Yuanrong Bao]. Writing-review and editing, supervision, resources, project administration, conceptualization: [Fei Jiao].

Conflicts of interest

The authors have no conflicts of interest to declare.

Data availability

The data supporting this study's findings are included within the article and its supplementary information (SI). Supplementary information is available. See DOI: https://doi.org/10.1039/d5ra08134c.

Acknowledgements

This research was supported by the National Key R&D Program of China (No. 2022YFF1202700) and the Fundamental Research Funds for the Central Universities.

References

1 T. W. Ebbesen, H. J. Lezec, H. Hiura, J. W. Bennett, H. F. Ghaemi and T. Thio, Electrical conductivity of individual carbon nanotubes, *Nature*, 1996, **382**, 54–56.
2 K. Suemori, Y. Watanabe and S. Hoshino, Carbon nanotube bundles/polystyrene composites as high-performance flexible thermoelectric materials, *Appl. Phys. Lett.*, 2015, **106**(11), 113902.

3 K. Oyaizu and H. Nishide, Radical polymers for organic electronic devices: a radical departure from conjugated polymers, *Adv. Mater.*, 2009, **21**(22), 2339–2344.
4 G. E. Rudebusch, J. L. Zafra, K. Jorner, K. Fukuda, J. L. Marshall, I. Arrechea-Marcos, G. L. Espejo, R. P. Ortiz, C. J. Gómez-García, L. N. Zakharov, M. Nakano, H. Ottosson, J. Casado and M. M. Haley, Diindeno-fusion of an anthracene as a design strategy for stable organic biradicals, *Nat. Chem.*, 2016, **8**(8), 753–759.
5 S. Zhang, H. Wang, J. Fu and G. Chen, Flexible films of poly(3,4-ethylenedioxythiophene):poly(styrenesulfonate)/ single-walled carbon nanotube/MXene thermoelectric composites and their devices, *Energy Mater. Adv.*, 2025, **6**, 0143.
6 L. Wang, C. Pan, Z. Chen, W. Zhou, C. Gao and L. Wang, Enhanced thermoelectric performance of conjugated polymer/single-walled carbon nanotube composites with strong stacking, *ACS Appl. Energy Mater.*, 2018, **1**(9), 5075–5082.
7 K. Choi, J. Son, Y. T. Park, J. S. Cho and C. Cho, Effect of the conformation changes of polyelectrolytes on organic thermoelectric performances, *Macromol. Res.*, 2020, **28**(11), 997–1002.
8 Z. Liu, C. Chen, J. Liu, Q. Sun, B. Huo, C. Du and G. Chen, All-day solar power generation enabled by photo/thermoelectric conversion and thermal energy storage, *Sci. China:Chem.*, 2025, **68**(5), 2035–2043.
9 C. Cho, B. Stevens, J. H. Hsu, R. Bureau, D. A. Hagen, O. Regev, C. Yu and J. C. Grunlan, Completely organic multilayer thin film with thermoelectric power factor rivaling inorganic tellurides, *Adv. Mater.*, 2015, **27**(19), 2996–3001.
10 D. L. Stevens, G. A. Gamag, Z. Ren and J. C. Grunlan, Salt doping to improve thermoelectric power factor of organic nanocomposite thin films, *RSC Adv.*, 2020, **10**(20), 11800–11807.
11 J. Sun, M. L. Yeh, B. J. Jung, B. Zhang, J. Feser, A. Majumdar and H. E. Katz, Simultaneous increase in seebeck coefficient and conductivity in a doped poly(alkylthiophene) blend with defined density of states, *Macromolecules*, 2010, **43**(6), 2897–2903.
12 Y. T. Park, A. Y. Ham and J. C. Grunlan, High electrical conductivity and transparency in deoxycholate-stabilized carbon nanotube thin films, *J. Phys. Chem. C*, 2010, **114**(14), 6325–6333.
13 P. T. Hammond, Form and function in multilayer assembly: new applications at the nanoscale, *Adv. Mater.*, 2004, **16**(15), 1271–1293.
14 Y. Bao, Y. Sun, F. Jiao and W. Hu, Enhanced thermoelectric performance of vapor phase polymerized PEDOT-Tos via ionic liquid post-treatment, *Adv. Sustainable Syst.*, 2024, **8**(9), 2400134.
15 C. Gayner and Y. Amouyal, Energy filtering of charge carriers: current trends, challenges, and prospects for thermoelectric materials, *Adv. Funct. Mater.*, 2020, **30**(18), 1901789.
16 P. P. Murmu, V. Karthik, Z. Liu, V. Jovic, T. Mori, W. L. Yang, K. E. Smith and J. Kennedy, Influence of carrier density and energy barrier scattering on a high Seebeck coefficient and power factor in transparent thermoelectric copper iodide, *ACS Appl. Energy Mater.*, 2020, **3**(10), 10037–10044.
17 J. Kennedy, P. P. Murmu, P. Kumar and G. Ramanath, Multifold enhancements in thermoelectric power factor in isovalent sulfur doped bismuth antimony telluride films, *Mater. Res. Bull.*, 2021, **142**, 111426.
18 C. Bounioux, P. Diaz-Chao, M. Campoy-Quiles, M. Martin-Gonzalez, A. Goni, R. Yerushalmi-Rozene and C. Mueller, Thermoelectric composites of poly(3-hexylthiophene) and carbon nanotubes with a large power factor, *Energy Environ. Sci.*, 2013, **6**(3), 918–925.
19 C. A. Hewitt, A. B. Kaiser, S. Roth, M. Craps, R. Czerw and D. L. Carroll, Varying the concentration of single walled carbon nanotubes in thin film polymer composites, and its effect on thermoelectric power, *Appl. Phys. Lett.*, 2011, **98**(18), 183110.
20 K. Suemori, S. Hoshino and T. Kamata, Flexible and lightweight thermoelectric generators composed of carbon nanotube-polystyrene composites printed on film substrate, *Appl. Phys. Lett.*, 2013, **103**(15), 153902.
21 O. Bubnova, Z. U. Khan, H. Wang, S. Braun, D. R. Evans, M. Fabretto, P. Hojati-Talemi, D. Dagnelund, J. B. Arlin, Y. H. Geerts, S. Desbief, D. W. Breiby, J. W. Andreasen, R. Lazzaroni, W. M. Chen, I. Zozoulenko, M. Fahlman, P. J. Murphy, M. Berggren and X. Crispin, Semi-metallic polymers, *Nat. Mater.*, 2014, **13**(2), 190–194.
22 J. Luo, D. Billep, T. Blaudeck, E. Sheremt, R. D. Rodriguez, D. R. Zahn, M. Toader, M. Hietschold, T. Otto and T. Gessner, Chemical post-treatment and thermoelectric properties of poly(3,4-ethylenedioxylthiophene):poly(styrenesulfonate) thin films, *J. Appl. Phys.*, 2014, **115**(5), 054908.
23 M. Kong, Q. Jiang, W. Zhong, Z. Wang, Y. Ma, G. Chen and J. He, Unraveling the correlation between reduced thickness and enhanced electrical conductivity in HNO_3-treated PEDOT:PSS ultrathin nanofilms, *Mater. Today Nano*, 2025, **29**, 100574.
24 Y. Bao, Y. Sun, F. Jiao and W. Hu, Recent advances in multicomponent organic composite thermoelectric materials, *Adv. Electron. Mater.*, 2023, **9**(5), 2201310.
25 Q. Jiang, J. Yang, P. Hing and H. Ye, Recent advances, design guidelines, and prospects of flexible organic/inorganic thermoelectric composites, *Mater. Adv.*, 2020, **1**(5), 1038–1054.
26 B. Russ, M. J. Robb, F. G. Brunetti, P. L. Miller, E. E. Perry, S. N. Patel, V. Ho, W. B. Chang, J. J. Urban, M. L. Chabinyc, C. J. Hawker and R. A. Segalman, Power factor enhancement in solution-processed organic n-type thermoelectrics through molecular design, *Adv. Mater.*, 2014, **26**(21), 3473–3477.
27 L. E. Bell, Cooling, heating, generating power, and recovering waste heat with thermoelectric systems, *Science*, 2008, **321**(5895), 1457–1461.

28 C. Cho, M. Culebras, K. L. Wallace, Y. Song, K. Holder, J. H. Hsu, C. Yu and J. C. Grunlan, Stable n-type thermoelectric multilayer thin films with high power factor from carbonaceous nanofillers, *Nano Energy*, 2016, **28**, 426–432.

29 S. Wang, S. Wang, D. Xu, H. Ding, J. Xie, Y. Jiang, C. Liu and Q. Huang, Multifunctional composite phase change material with electrostatic self-assembly structure based on carboxylated multi-walled carbon nanotubes, *Carbon*, 2025, **231**, 119763.

30 X. Zhang, M. Chen, Y. Yu, T. Yang and J. Wang, Polyelectrolyte-modified multi-walled carbon nanotubes for the adsorption of chromium (vi), *Anal. Methods*, 2011, **3**(2), 457–462.

31 N. Toshima, K. Oshima, H. Anno, T. Nishinaka, S. Ichikawa, A. Iwata and Y. Shiraishi, Novel hybrid organic thermoelectric materials: three-component hybrid films consisting of a nanoparticle polymer complex, carbon nanotubes, and vinyl polymer, *Adv. Mater.*, 2015, **27**(13), 2246–2251.

32 Z. Fan and J. Ouyang, Thermoelectric properties of PEDOT:PSS, *Adv. Electron. Mater.*, 2019, **5**(11), 1800769.

33 X. Crispin, S. Marciniak, W. Osikowicz, G. Zotti, A. D. Van Der Gon, F. Louwet, M. Fahlman, L. Groenendaal, F. De Schryver and W. R. Salaneck, Conductivity, morphology, interfacial chemistry, and stability of poly(3,4-ethylene dioxythiophene)-poly(styrene sulfonate): a photoelectron spectroscopy study, *J. Polym. Sci., Part B:Polym. Phys.*, 2003, **41**(21), 2561–2583.

34 G. Tan, L. D. Zhao and M. G. Kanatzidis, Rationally designing high-performance bulk thermoelectric materials, *Chem. Rev.*, 2016, **116**(19), 12123–12149.

35 Y. Yamashita, J. Tsurumi, M. Ohno, R. Fujimoto, S. Kumagai, T. Kurosawa, T. Okamoto, J. Takeya and S. Watanabe, Efficient molecular doping of polymeric semiconductors driven by anion exchange, *Nature*, 2019, **572**(7771), 634–638.

36 N. Saxena, B. Pretzl, X. Lamprecht, L. Biessmann, D. Yang, N. Li, C. Bilko, S. Bernstorff and P. Müller-Buschbaum, Ionic liquids as post-treatment agents for simultaneous improvement of Seebeck coefficient and electrical conductivity in PEDOT: PSS films, *ACS Appl. Mater. Interfaces*, 2019, **11**(8), 8060–8071.

37 A. Fraleoni-Morgera and M. Chhikara, Polymer-based nanocomposites for thermal insulation, *Adv. Eng. Mater.*, 2019, **21**(7), 1801162.

38 Y. Zheng, Z. Yang, Z. Li, W. Liu, C. Yang, J. Shen, H. Wang, K. Xu, L. Cheng, R. Zhang and Z. Jiang, Polyelectrolyte-modified covalent organic framework membranes for multivalent cation removal, *J. Membr. Sci.*, 2025, **713**, 123363.

39 B. P. Tripathi, N. C. Dubey and M. Stamm, Functional polyelectrolyte multilayer membranes for water purification applications, *J. Hazard. Mater.*, 2013, **252**, 401–412.

40 W. Zhou, Q. Fan, Q. Zhang, L. Cai, K. Li, X. Gu, F. Yang, N. Zhang, Y. Wang, H. Liu, W. Zhou and S. Xie, High performance and compact-designed flexible thermoelectric modules enabled by a reticulate carbon nanotube architecture, *Nat. Commun.*, 2017, **8**(1), 14886.

41 H. Z. Geng, K. K. Kim, K. P. So, Y. S. Lee, Y. Chang and Y. H. Lee, Effect of acid treatment on carbon nanotube-based flexible transparent conducting films, *J. Am. Chem. Soc.*, 2007, **129**(25), 7758–7759.